

Spurious Rollover of Wave Attenuation Rates in Sea Ice Caused by Noise in Field Measurements



†Deceased.

 Jim Thomson^{1,2} , Lucia Hošeková^{1,3} , Michael H. Meylan⁴ , Alison L Kohout⁵, and Nirnimesh Kumar^{2,†}
Key Points:

- Noise in raw wave data adds spurious energy to observed wave spectra
- The noise energy causes a bias in the attenuation rates inferred from observed wave spectra
- The bias is a strong function of frequency and explains the rollover in attenuation rates reported in several previous studies

Correspondence to:
 J. Thomson,
jthomson@apl.washington.edu
Citation:
 Thomson, J., Hošeková, L., Meylan, M. H., Kohout, A. L., & Kumar, N. (2021). Spurious rollover of wave attenuation rates in sea ice caused by noise in field measurements. *Journal of Geophysical Research: Oceans*, 126, e2020JC016606. <https://doi.org/10.1029/2020JC016606>

 Received 17 JUL 2020
 Accepted 5 FEB 2021

¹Applied Physics Laboratory, University of Washington, Seattle, WA, USA, ²Department of Civil and Environmental Engineering, University of Washington, Seattle, WA, USA, ³Department of Meteorology, University of Reading, Reading, UK, ⁴School of Mathematical and Physical Sciences, The University of Newcastle, Callaghan, NSW, Australia, ⁵National Institute of Water and Atmospheric Research, Christchurch, New Zealand

Abstract The effects of instrument noise on estimating the spectral attenuation rates of ocean waves in sea ice are explored using synthetic observations in which the true attenuation rates are known explicitly. The spectral shape of the energy added by noise, relative to the spectral shape of the true wave energy, is the critical aspect of the investigation. A negative bias in attenuation that grows in frequency is found across a range of realistic parameters. This negative bias decreases the observed attenuation rates at high frequencies, such that it can explain the rollover effect commonly reported in field studies of wave attenuation in sea ice. The published results from five field experiments are evaluated in terms of the noise bias, and a spurious rollover (or flattening) of attenuation is found in all cases. Remarkably, the wave heights are unaffected by the noise bias, because the noise bias occurs at frequencies that contain only a small fraction of the total energy.

Plain Language Summary Many previous studies have determined the rate at which ocean surface waves decay as they travel through sea ice. This work identifies a systematic bias in those results, using both published data and synthetic data to demonstrate the effect. The bias addresses a long-running debate on the details of how waves decay in sea ice.

1. Introduction

Ocean surface wave attenuation in sea ice is an established phenomenon (Squire, 2007, 2020) and has been extensively studied using field measurements of wave energy E as a function of frequency f . The attenuation of spectral wave energy $E(f)$ is often expressed as an exponential decay with distance x , such that

$$E(f, x) = E(f, 0)e^{-\alpha(f)x}. \quad (1)$$

The attenuation rate α controls the reduction of wave energy from the incident waves in open water ($x = 0$) to some position within the sea ice. The attenuation rate is then a function of frequency, most commonly a power law,

$$\alpha(f) = af^b, \quad (2)$$

where a and b are constants determined for different ice types during previous studies. Meylan et al. (2018) provide a comprehensive review of the frequency dependence of $\alpha(f)$.

Although $\alpha(f)$ is generally thought to increase with frequency f , many field experiments have suggested a “rollover” in which $\alpha(f)$ eventually decreases at the highest frequencies. These are frequencies commonly referred to as the “tail” of the wave energy spectrum. Wadhams (1975) first noted the rollover, and it was described more fully in the seminal work of Wadhams et al. (1988), who find a rollover in the spectral attenuation rates across many experiments with varying ice types and wave conditions. The rollover is challenging to diagnose because most field observations simply provide the ratio of energy at different locations $E(f, x_1)$, $E(f, x_2)$ and not the actual loss of energy caused by the sea ice. Wadhams et al. (1988) describes two possible mechanisms that might cause the observed rollover, both of which essentially replace (or input)

© 2021. The Authors.

This is an open access article under the terms of the [Creative Commons Attribution-NonCommercial License](https://creativecommons.org/licenses/by-nc/4.0/), which permits use, distribution and reproduction in any medium, provided the original work is properly cited and is not used for commercial purposes.

some of the wave energy at high frequencies: (1) input of additional wave energy by wind, and (2) nonlinear transfer of wave energy from lower frequencies to higher frequencies. Masson and LeBlond (1989) consider this further and suggest that winds can input considerable energy into waves in partial ice cover. The various field experiments in Wadhams et al. (1988) data set report the rollover effect in a range of conditions, including very light winds and small waves with little likelihood of significant nonlinearity. The ubiquity of the rollover is difficult to explain by the two above mechanisms alone.

Recent work has explored both mechanisms suggested by Wadhams et al. (1988), including a more thorough framework for nonlinear transfers (Polnikov & Lavrenov, 2007) and testing wind input effects (Li et al., 2017; Rogers et al., 2016). Particularly, Li et al. (2017) provide a comprehensive treatment of wind input using modern field observations and a spectral wave model. They conclude that wind input at high frequencies is sufficient to replace some of the wave energy attenuated at high-frequencies, such that re-analysis of the data no longer indicates a rollover in the spectral attenuation rates (though a rollover does appear without considering wind input).

Here, we explore instrument noise as another possible explanation for the emergence of spurious rollovers in attenuation rates from field experiments. Assuming that the noise in the raw data are random errors with Gaussian statistics, the noise will contribute additional variance to the raw data, and this will elevate the spectral wave energy densities $E(f, x)$ determined from the raw data. In terms of variance, this bias in energy will always be positive, even though the actual errors are symmetric with zero-mean. According to the Bienayme theorem, the total variance (energy) will be the sum of the true variance from the wave signal and the variance from the noise because there are no cross-terms from these uncorrelated signals. Following Parseval's theorem, this variance is preserved in the calculation of frequency spectra, such that

$$E(f, x) = E_s(f, x) + E_n(f) \quad (3)$$

The observed wave energy spectra $E(f, x)$ is thus a sum of the energy in the wave signal $E_s(f, x)$ and the variance added by instrument noise $E_n(f)$. Although the assumption of Gaussian errors in the raw data would result in a constant “white” spectral shape for $E_n(f)$, the effects of filters and other processing may produce an $E_n(f)$ that is a strong function of frequency. This will be explored in the Methods section.

Previous studies have been well-aware of instrument noise and typically applied cutoff levels below which $E(f, x)$ observations are not used. However, the spectral shape of the noise energy $E_n(f)$ and effects on inferred attenuation rarely have been considered. Most importantly, the value of $E_n(f)$ will remain at the same level while $E_s(f, x)$ decreases with x due to attenuation by sea ice, such that the relative amount of noise increases with distance. For example, Cheng et al. (2017) tried to avoid noise contamination by using a constant cutoff of $E(f, x) > 10^{-5} \text{ m}^2/\text{Hz}$ in processing data from the Arctic Sea State experiment (Thomson, Ackley, et al., 2018). This choice of noise floor is coincidentally the same as the cutoff in (Wadhams et al., 1988). Even though Cheng et al. (2017) did not observe a rollover, they did find a flattening of attenuation rate α at high frequencies and large distances, which they attributed to wind input. More critically, Meylan et al. (2014) did not see a rollover in attenuation rates when analyzing Antarctic wave data with a constant cutoff level of $E(f, x) > 10^{-2}$, yet Li et al. (2017) analyzed the same data with a much lower cutoff and did see a strong rollover in attenuation rate. A notable exception is Sutherland et al. (2018), who treat spectral noise explicitly and do not infer a rollover in attenuation.

Here, we present a framework to understand the bias in attenuation caused by the spectral slope of energy from noise $E_n(f)$ relative to the spectral slope of energy from the wave signal $E_s(f)$. We revisit five different field experiments from the literature to test assumptions about the shape of $E_n(f)$ and look for empirical evidence in the observed energy spectra. We then create synthetic wave energy spectra with known spectral attenuation rates, and then explore the inferred attenuation rates after the variance from instrument noise is added to the synthetic spectra. The general parametric form of bias in attenuation is also derived. The discussion focuses on the spurious nature of previous “rollover” results and presents recommendations for avoiding noise bias in using field observations of wave spectra in ice. Except for a brief aside in the Discussion section regarding low frequencies, we focus entirely on the high frequency tail of the energy spectra.

Table 1
Case Studies and Input Parameters for Spectral Noise Effects

Case	H_s [m]	a	b	H_n [m]	r	x [m]
CODA 2019	0.5 to 2.5	0.026	2.7	0.08	−4	0 to 6×10^3
SeaState 2015	0.1 to 4.0	0.015	3.0	0.03	−4	0 to 100×10^3
SIPEX 2012	0.1 to 6.0	0.005	2.0	0.03	−4	16 to 130×10^3
STiMPI 2000	0.1 to 5.0	0.010	2.9	0.15	−4	10 to 80×10^3
Greenland Sea 1978	0.5 to 1.5	0.020	3.6	0.01	0, −4	0 to 50×10^3

True attenuation rates are specified as $\alpha_t(f) = af^b$.

2. Methods

2.1. Specification of Case Studies

Case studies are chosen to span a wide range of methodologies and published spectral attenuation rates. Not all of these cases reported a complete rollover in published attenuation rates; the intent is to show the full range of noise effects on attenuation estimates. A realistic true attenuation rate $\alpha_t(f) = af^b$ is specified for each case study, and this is used to create synthetic (true) spectra to which noise is then added. Table 1 summarizes the conditions and parameters for each case study, which are referred to by experiment name, rather than the publication(s) of those results.

The first two case studies use observations from SWIFT buoys (Thomson, 2012), which use GPS velocities in onboard processing (Herbers et al., 2012) and accelerometer data in postprocessing. The first case was collected in 2019 along the coast of Alaska in pancake ice as part of the Coastal Ocean Dynamics in the Arctic (CODA) program (Hosekova et al., 2020). The second case was collected in 2015 in the Beaufort Sea in pancake ice as part of the Arctic Sea State program (Cheng et al., 2017; Rogers et al., 2016; Thomson, Ackley, et al., 2018). The third case uses observations from custom buoys during SIPEX in the Antarctic Marginal Ice Zone (MIZ) in 2012, as described in Kohout et al. (2014); Kohout et al. (2015). The fourth case uses observations from custom buoys during STiMPI in the Weddell Sea in pancake ice in 2000, as described in Doble et al. (2015). Finally, the Greenland Sea September 16, 1978 experiment from Wadhams et al. (1988) is used as a fifth case study.

2.2. Spectral Energy of the Wave Signal, $E_s(f)$

Ocean waves typically have an energy spectrum with a power law in the spectral tail (i.e., frequencies above the peak frequency f_p) and the overall level can be described by the conventional definition of the significant wave height H_s ,

$$E_s(f > f_p, x) \sim f^q \quad H_s = 4\sqrt{\int E_s(f) df}. \quad (4)$$

In open water, we expect the familiar shape $q = -4$ of the equilibrium tail (Lenain & Melville, 2017; Phillips, 1985; Thomson et al., 2013). Figure 1 shows the energy spectra from observations in the four case studies, which are bin-averaged by H_s and presented in logarithmic space to visualize the f^q dependence. The $q = -4$ shape is clear for open water observations (which are the largest H_s bins) in the CODA 2019 and SeaState 2015 case studies. This $q = -4$ shape in the spectrum is related to a wave field with constant geometric steepness of the waves themselves, expressed as a spectrum of mean-square-slope $mss(f) = E_s(f) f^4$ that has a constant level in f (see Thomson et al., 2013).

In sea ice, the spectral shape is typically observed to be much steeper ($q < -4$), which is consistent with largest H_s bins in the SIPEX 2012 and STiMPI 2000 case studies (Figure 1). These experiments did not include wave observations in open water, so all wave spectra already have slopes $q < -4$. This high-frequency tail and the implied changes for wave steepness are the focus of the present study.

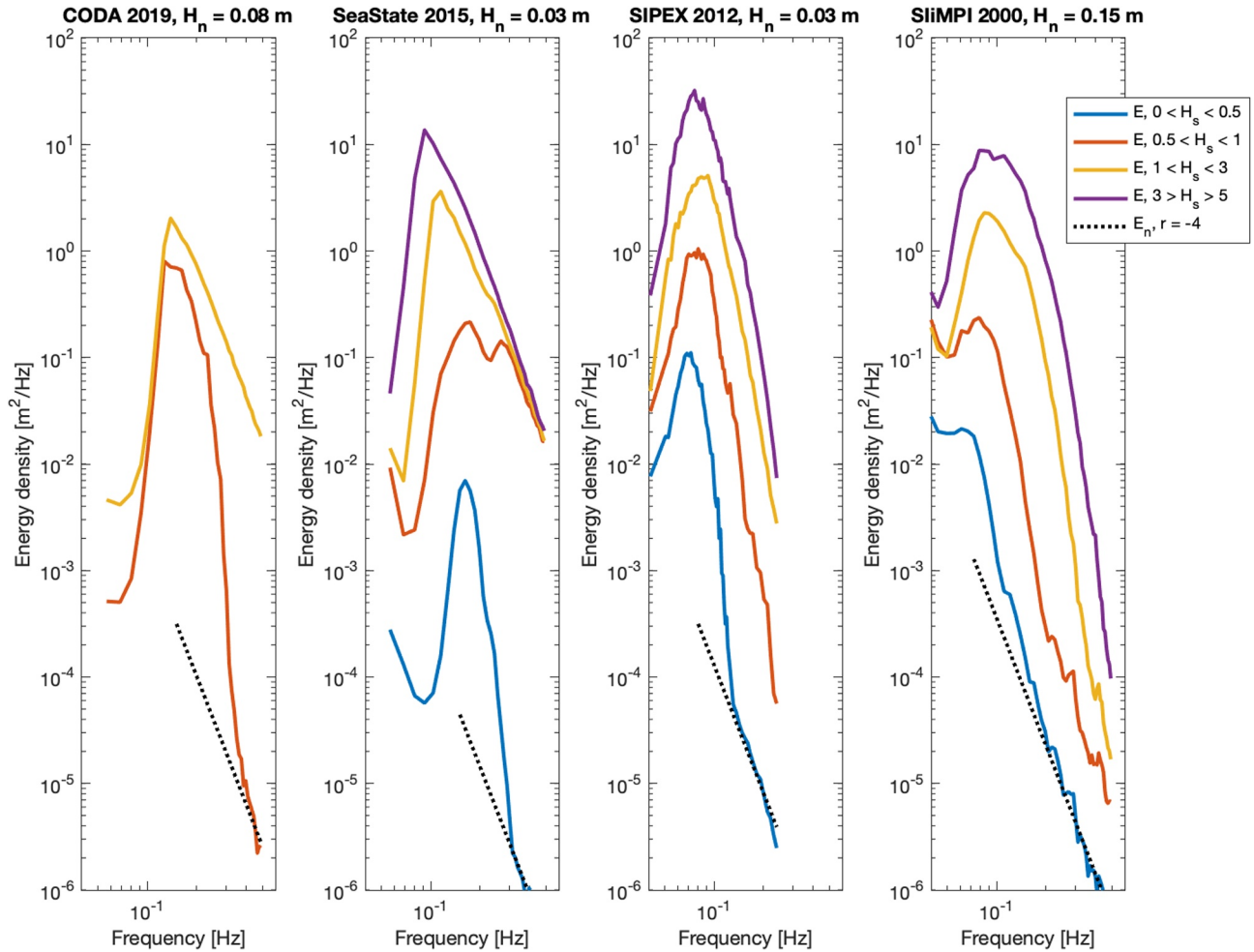


Figure 1. Wave spectra from actual field observations (not synthetic) during four case studies. Spectra are binned by wave height (see legend), and a dotted black line shows the estimated noise energy following Equation 5.

Lacking access to the actual data, we cannot include the Greenland Sea 1978 spectra in Figure 1. We can, however, reconstruct the conditions using parametric spectra to match the incident energy levels in Wadhams et al. (1988) and proceed to explore the implications of the reported $E_n(f) = 10^{-5} \text{ m}^2/\text{Hz}$ noise floor and the possibility of a frequency dependence in this noise.

The ensemble average spectra in Figure 1 have nonstationary conditions, and thus are not valid determinations of the spectral shape of the wave energy. However, the spectral energy contributed from noise is independent of the wave signal and should have stationarity over all conditions. Thus, Figure 1 includes robust ensembles of the noise spectra, which emerge as the dominant signal in the higher frequencies whenever the waves are small. More details follow.

2.3. Spectral Energy of Noise, $E_n(f)$

There is additional variance (energy) from noise $E_n(f)$ in observed wave spectra, following Equation 3. We assume energy from noise follows power law in the spectral tail (i.e., frequencies above the peak frequency f_p) and we scale the level with a noise height H_n (analogous to significant wave height):

$$E_n(f > f_p) \sim f^r, \quad H_n = 4\sqrt{\int E_n(f) df}. \quad (5)$$

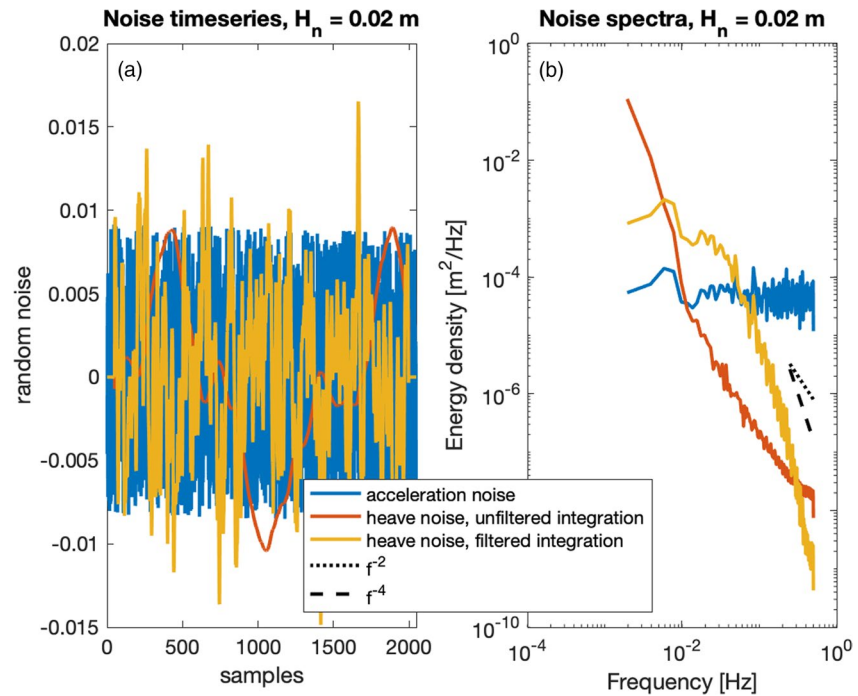


Figure 2. Demonstration of (a) time series and (b) spectra of random noise (blue curves), that is double-integrated without a filter (red curves) and double integrated with a high-pass filter (yellow curves).

The noise height H_n is thus four times the standard deviation of the Gaussian random noise embedded in the raw wave elevations. Note, again, that the effect of noise in the raw data is to increase the total variance, such that the noise height H_n is a bias in the true wave height H_s , not a symmetric error.

The noise height H_n is used as a general characterization of the level of noise $E_n(f)$, though wave elevations rarely are measured directly. The type of sensor used for the raw measurements and the subsequent processing to estimate wave elevations will control the frequency exponent r . The expected exponents are $r = -4$ for the double-integration of accelerometers, or $r = -2$ for the single-integration of GPS velocities, or $r = 0$ (white noise) from direct measurements of heave (such as from an altimeter or LIDAR). For accelerometers, each integration in time is equivalent to a factor f^{-1} , and then the f^{-2} effect from double integration is squared to get f^{-4} when calculating energy (instead of amplitude).

Figure 2 demonstrates the effects of integration and filtering on a synthetic signal that begins as a random noise time series. The double integration always causes a negative slope ($r < 0$) in the energy spectra of the noise, but the details of the shape are sensitive to filters applied during the double integration. Here, a simple RC filter is applied to prevent the accumulation of errors in the double integration (see Equations 2 and 3 in Thomson, Garton, et al., (2018)). This is the same filter for the SWIFT buoys in the CODA 2019 and SeaState 2015 studies. In other buoys, such filtering is often a black-box running onboard the motion sensor itself. High-pass filters often have dynamic (and nonlinear) responses, which makes it difficult to determine a universal noise contribution to computed energy spectra. Still, we can expect a universal form $E_n \sim f^r$ with $r < 0$ in the high-frequency tail. The low-frequency region is more challenging to determine a canonical form; those effects are largely beyond the scope of the present work.

Figure 1 includes dotted lines for the spectral shape of energy from noise $E_n(f)$ for each case study, with corresponding H_n values estimated from sensor specifications (or from collecting raw data on land with a stationary buoy). For each experiment, the wave spectra in Figure 1 show the clear effects of the noise energy as a change in the slope of the spectra at the higher frequencies of the smallest H_s bin. These shapes are consistent with accelerometer noise that begins as purely random (white) noise and becomes $r = -4$ with double integration in time (and filtering). This noise energy is always present in the energy spectra,

but it only becomes noticeable when wave energy is small. Thus, when H_s is small, $E_n(f) > E_s(f)$ at the higher frequencies, even though $H_n < H_s$.

Lacking observed estimate of $E_n(f)$ for the Greenland Sea case (excluded from Figure 1), we will apply the reported constant noise floor of $E_n(f) = 10^{-5} \text{ m}^2/\text{Hz}$ and explore both the implied noise shape $r = 0$, as well as the more likely $r = -4$. We use a $H_n = 1 \text{ cm}$ consistent with the implied total noise variance of the reported constant $E_n(f)$. We note that the reported noise level (and equivalent H_n) from Wadhams et al. (1988) is rather optimistic, relative to the other experiments with modern instrumentation in Table 1, but we retain the reported value for consistency.

As brief aside, we consider the alternate interpretation of the change in the slope of the $E(f)$ tail for small H_s in Figure 1. Since the geometric (i.e., crest to trough) steepness of the waves is set by the fourth moment of the spectrum (Banner, 1990), a true change in the $E(f)$ tail would require the highest frequency waves to become abruptly steeper. As there are no visual observations to support such a change in the crest-to-trough shape of the shortest waves, we reject this interpretation and proceed with interpreting the change in the slope of the $E(f)$ tail when H_s is small as an indication of noise exceeding signal.

The noise energy at low frequencies is not well-constrained, and the results that follow will be restricted to the high frequencies ($f > f_p$) for which the roll-over of attenuation has been so commonly reported. The low frequencies likely are sensitive to filtering, as is hinted by the shifting inflection points for $f < f_p$ in the Sea State 2015 data set for different bins of wave height.

The additional energy from the instrument noise $E_n(f)$ makes it impossible to measure energy less than the dotted lines, so when the wave signal $E_s(f)$ becomes weak at high frequencies, the observed spectra $E(f)$ converge to the dotted lines of $E_n(f)$. When waves are larger, the noise energy is a negligible fraction of the total energy, and the effects are not readily detected in the spectral shape. Although both CODA 2019 and SeaState 2015 use SWIFT buoys, the effective H_n is different between these experiments because of different filters used to suppress low-frequency drift during the double integration of accelerometer data. Although both the SeaState 2015 and SIPEX 2012 data sets have $H_n = 3 \text{ cm}$, the spectral levels of $E_n(f)$ are slightly different because the processed spectra have different resolution in frequency df (see Equation 5). Although all of the experiments in Figure 1 use accelerometer measurements with an effective $r = -4$ shape in noise energy, it is important to note that other experiments may have different measurements. One such example is Ardhuin et al. (2020), who use GPS velocities as the raw data and thus likely have noise energy with an $r = -2$ shape.

2.4. Synthetic Spectra

In the synthetic tests that follow, the incident open-water wave spectra $E_s(f, x = 0)$ are specified using Pierson–Moskowitz spectra for fully developed seas, following Alves et al. (2003). In open water, this $q = -4$ (Equation 4) shape is known to persist even in the case of a pure swell without wind (Vincent et al., 2019), though the Pierson–Moskowitz spectra was developed for a pure wind sea. The synthetic wave spectra use a frequency range of $0.05 < f < 0.5 \text{ Hz}$ and a resolution $df = 0.01 \text{ Hz}$, which is similar to many modern wave buoys.

A given incident wave spectrum $E(f, 0) = E_s(f, 0) + E_n(f)$, designed to match a given case study, is attenuated with distance x into the ice at regular intervals similar to the measurements from that case study. This noise is not cumulative in x and is assumed independent of the wave signal; it is a specified additional spurious energy for each observation $E(f, x)$. Using a specified (true) attenuation rate $\alpha_r(f)$ with a frequency exponent b (Equation 1), a true wave spectrum $E_s(f, x)$ at each distance is obtained. This true spectrum already includes the energy from noise $E_n(f)$ added in the incident wave spectrum at $x = 0$ (Equation 4), but it does not include the energy from noise of the other measurement at position x . That noise energy is explicitly added to create total spectra, $E(f, x)$, following Equation 3. The key point is that the energy of the noise does not decay with distance x , though the wave energy does, and each total spectrum has noise energy added independently. The noise energy added to the incident wave spectrum $E(f, 0)$ likely has negligible effects because the wave energy is generally much larger than the noise energy in defining $E(f, 0)$ at the ice edge. Farther into the ice, however, the noise energy in any particular measurement may be a much more significant fraction of the observed energy $E(f, x)$, especially for the higher frequencies.

2.5. Inferred Attenuation Rates from Spectra with Noise

Using the synthetic spectra (with added noise), inferred attenuation rates are determined using Equation 1 rearranged as

$$\alpha(f) = -\frac{1}{x_2 - x_1} \ln \left(\frac{E(f, x_2)}{E(f, x_1)} \right) \quad (6)$$

and least-squares fitting the synthetic $E(f, x)$ at each frequency f using pairs of positions x_1, x_2 . Using $x_1 = 0$ is most consistent with the definition in Equation 1, however, this is not always measured in field experiments and we instead use the more general case of fitting all x_1, x_2 pairs for which $x_2 > x_1$. There are several other options for fitting Equation 1, though the choice of the fitting method is not important for the present study, given that true attenuation rates are known a priori. Inferred attenuation is then compared with the true attenuation that was specified in producing the synthetic results, especially in regards to frequency dependence. The overall frequency dependence b is inferred by least-squares fitting Equation 2 with

$$b = \frac{\ln f}{\ln(\alpha(f))} \quad (7)$$

from the peak frequency f_p of the incident spectrum $E(f, 0)$ to the max frequency observed $f = 0.5$ Hz. This inferred b is somewhat sensitive to the choice of frequency range for fitting, but it is only meant to show qualitative effects for values relevant to the case studies. Using frequencies $f > f_p$ centers the results on the tail of the wave energy spectrum, where rollovers have been reported in previous studies.

3. Results

The results begin with the general effect of the spurious variance (energy) added to observed wave energy spectra, followed by the case studies. The energy from noise causes substantial changes to the shape of the observed attenuation rates, in general, and for all the cases examined herein. The case studies provide both a practical sense of the problem, as well as an exploration of the parameter space that cannot be fully described by the assumptions in the general solution.

3.1. Generalized Effects of Noise

Combining Equations 1 and 3 gives the general form of the observed $\alpha(f)$ as a function of the true $\alpha_t(f)$ and the ratio of noise energy $E_n(f)$ to the true spectral energy of the wave signal $E_s(f)$,

$$\alpha(f) = \alpha_t(f) - \frac{1}{x} \ln \left(1 + \frac{E_n(f)}{E_s(f, x)} \right) \quad (8)$$

Previous studies have applied a uniform cutoff in $E(f, x)$ (with implied $r = 0$ in Equation 5) and discarded any attenuation calculated for $\frac{E_n(f)}{E_s(f, x)} > 1$. The problem is that such a ratio is unlikely to be constant in frequency. Even for ratios of $\frac{E(f_p)}{E_s(f_p, x)} \sim 1$, the absolute error in $\alpha(f)$ at any particular f may be small, but the error in the dependence on f may be severe (because the bias grows in f). In particular, if the spectral shapes of $E_n(f), E_s(f, x)$ diverge, the effects of noise energy will be a strong function of frequency.

Assuming that $E_s(f, x)$ and $E_n(f)$ are both power laws in f , the error in attenuation grows with approximately $\ln(f)$. The specific rate comes from the ratio of the power laws, which is almost assured to be positive given that $E_s(f, x)$ will only steepen from an initial $q = -4$. There are no known or proposed mechanisms for a natural wave energy spectrum ever to have a slope less than f^{-4} . The noise spectra have at most a slope

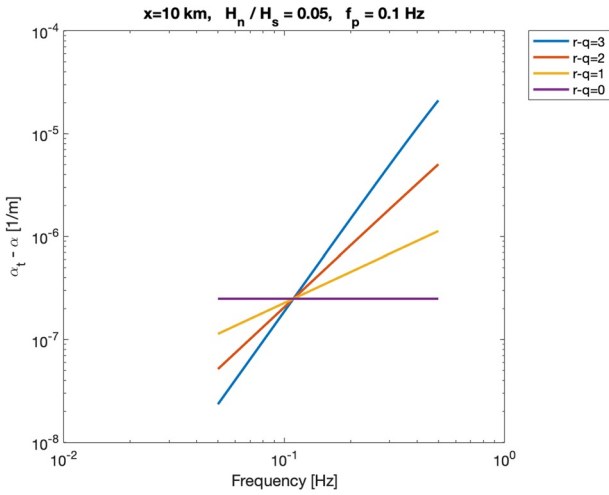


Figure 3. Bias in observed $\alpha(f)$ as a function of frequency for combined signal and noise exponents $r - q$. Example shown is for a distance of 10 km into the sea ice and a ratio of noise to true wave heights $H_n/H_s = 5\%$.

of $r = -4$ for accelerometer measurements and less for other methods. Thus, wave energy in sea ice will tend to decrease with frequency faster than the noise energy decreases with frequency, and a negative bias in attenuation that grows with frequency is almost assured.

The general form of the bias in attenuation is controlled by the ratio

$$\frac{E_n(f)}{E_s(f, x)} \sim f^{r-q}, \quad (9)$$

and thus for any $q < r$ the negative bias in attenuation will grow in frequency. Figure 3 illustrates the attenuation bias for $\frac{H_n}{H_s} = 0.05$ at the peak frequency f_p and various $r - q$ combinations. Given the typical range of $10^{-5} < \alpha(f) < 10^{-3}$, the errors for in Figure 3 are significant. For any attenuation that grows in frequency (Equation 2), the slope of $E_s(f, x)$ will become more and more negative in ice (i.e., $q < -4$) and thus for any reasonable range of noise shape ($-4 < r < 0$), the ratio will grow. Thus, it is only for the rare case of a constant true attenuation ($b = 0$) that maintains $q = -4$ within the ice and noise shape of $r = -4$ that the bias in observed attenuation will be constant. In some conditions, the

growing bias may only be sufficient to flatten the observed attenuation rates; in others, it will cause an apparent rollover in attenuation at high frequencies. This flattening is expected for the particular case of an open water $E(f, x = 0)$ that is used for all attenuation calculations, since both exponents q, r will tend to -4 .

Another mechanism by which $E_s(f, x)$ could retain the f^{-4} shape for all x is through wind input, which is often discussed in relation to the spectral shape of wave attenuation in sea ice. If wind input in sea ice was analogous to the equilibrium concepts of Phillips (1985), then $E_s(f, x) \sim f^{-4}$ could be maintained, even as the overall $E_s(f, x)$ was reduced by an attenuation that was not constant in frequency. Even with wind input, f^{-4} remains a bound on the slope of the true wave spectra. Figure 3 shows that even in such conditions, the negative bias in $\alpha(f)$ is likely to grow in frequency, and thus the shape of inferred $\alpha(f)$ will be altered.

The spatial dependence $\frac{1}{x}$ in Equation 8 is also worth noting, since it may cause severe bias at short distances even when the ratio $\frac{E_n(f)}{E_s(f, x)}$ is small. Indeed, Li et al. (2017) note changes in the rollover period for

different distances that may be related to the attenuation bias changing with $\frac{1}{x}$. Figure 3 uses a distance of $x = 10$ km, which is within the range of all field experiments discussed herein.

The role of distance and the effect of true spectra $E_s(f, x)$ that steepen beyond $q = -4$ within ice are explored in the case studies that follow, using the parameters in Table 1. There are figures and descriptions for each case, following a standard format. Each case has some range of x and f for which the noise has a strong effect on the inferred $\alpha(f)$. However, the significant wave heights are rarely affected by the noise, even far within the ice. The practical result is that noise energy remains a small fraction of the total energy for all cases, but it has significant effects on the spectral shape of inferred attenuation. In summary, noise can affect H_s no more than the value of H_n , but noise can make the apparent α go all the way to zero at high frequencies.

3.2. CODA 2019

The Chukchi Sea CODA 2019 case study results are shown in Figure 4. Panel (a) shows true spectra that steepen with distance into the ice, and panel (b) shows observed spectra that begin to approach the $r = -4$ noise floor slope at the highest frequencies. In panel (c), the attenuation rates estimated from the observations (Equation 6) have a negative bias that flattens the frequency response away from the true attenuation.

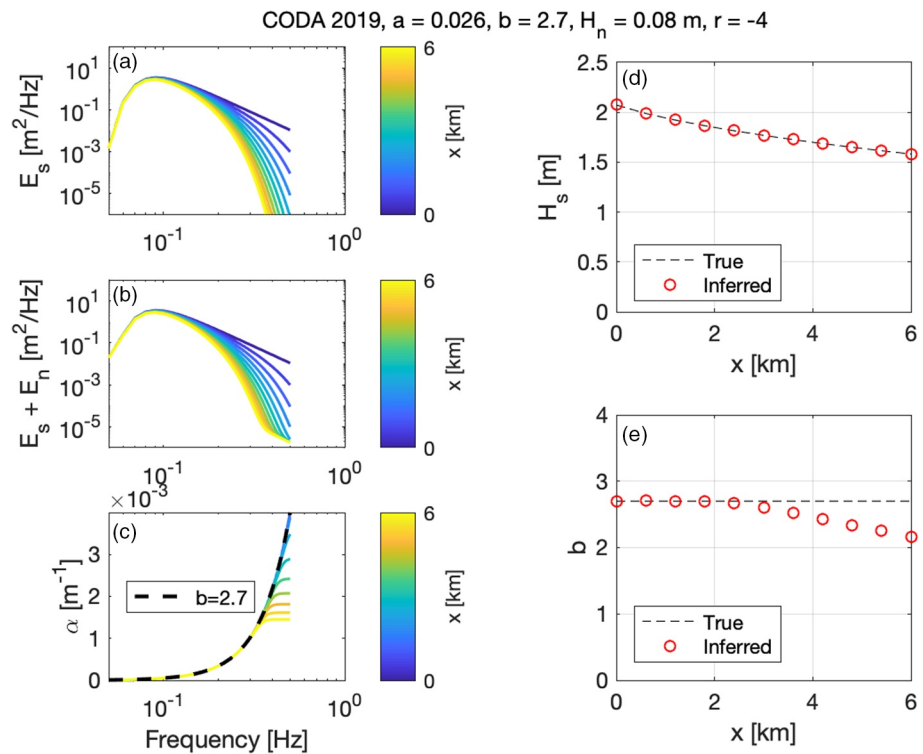


Figure 4. Synthetic results for the Chukchi Sea CODA 2019 case study. (a) True wave energy spectra (colors show distance into the ice). (b) Observed wave energy spectra with noise added (colors show distance into ice). (c) True attenuation rate (black dashed line) and observed attenuation rate (colors show distance into ice). (d) Wave heights as a function of distance into the ice that are specified as true (black dashed line) and observed (red circles). (e) Exponent of frequency power law in attenuation that is determined from observations (red circles) and specified as true (black dashed line).

Thus the fitted exponent shown in panel (e) deviates from the true $b = 2$ with increasing distance into the ice. In panel (d), the observed wave heights agree well with the true wave heights.

This case study is a best-case scenario, in which the negative bias in attenuation is small and limited to flattening $\alpha(f)$ at a few frequencies. This is because the noise is steep ($r = -4$) and the distances are short ($0 < x < 6$ km) such that the true energy spectra do not become much steeper than f^{-4} .

3.3. Sea State 2015

The Sea State 2015 case study results are shown in Figure 5. Panel (a) shows true spectra that steepen dramatically with the longer distances into the ice, and panel (b) shows observed spectra that clearly tend to the $r = -4$ noise floor slope at many frequencies. In panel (c), the attenuation rates estimated from the observations (Equation 6) have a negative bias that flattens the frequency response away from the true attenuation ($b = 3$). This trend is similar to the Cheng et al. (2017) results from analyzing the actual field data, in which a flattening of $\alpha(f)$ is evident for $f > 0.3$ Hz in their Figure 4. Cheng et al. (2017) attributed this flattening to wind input; here, we show that it is more likely caused by negative bias from spectral noise in the observations. In both the synthetic observations and the actual field observations, a full rollover in the observed α does not occur. The $r = -4$ shape of the noise is only sufficient to flatten α in frequency; a full rollover (decrease of $\alpha(f)$ in frequency) would require noise with a different shape (i.e., $r = -2$ or $r = 0$). As the spurious flattening of $\alpha(f)$ expands in frequency, the fitted exponent b shown in panel (e) deviates from the true $b = 2$ with increasing distance into the ice. Despite the noticeable bias in $\alpha(f)$, the observed wave heights agree well with the true wave heights (Figure 5d).

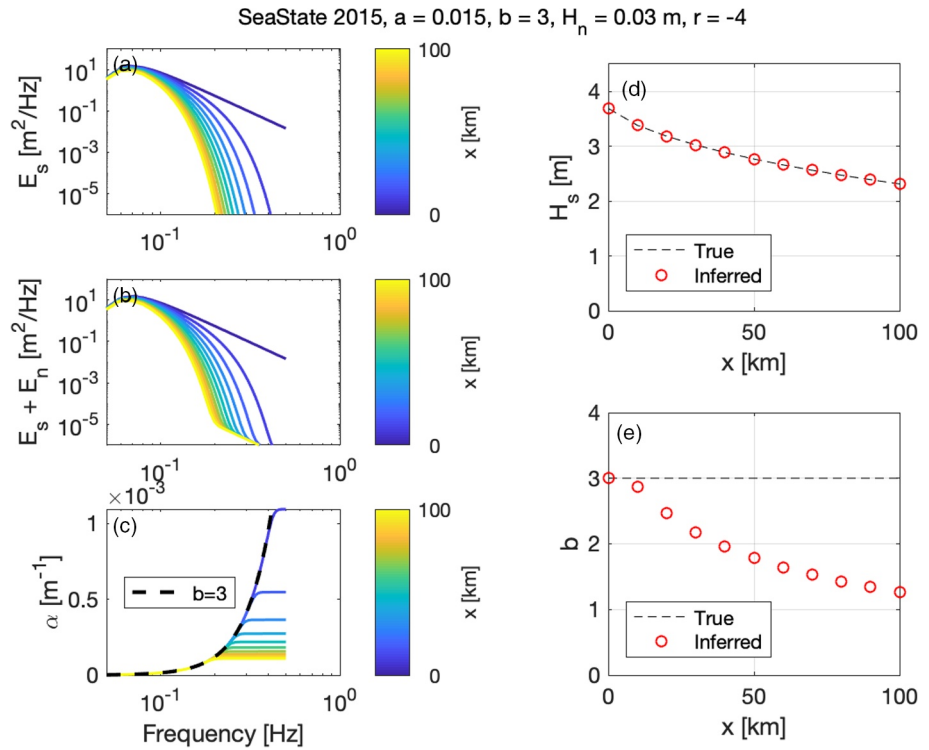


Figure 5. Synthetic results for the Beaufort Sea State 2015 case study. Panels as in Figure 4.

3.4. SIPEX 2012

The Antarctic MIZ 2012 case study results are shown in Figure 6. All of the observed spectra in panel (b) are effected by noise energy, even though the imposed noise height is only $H_n = 3$ cm. In panel (c), the observed attenuation rates have a clear rollover in frequency that is spurious relative to the $b = 2$ dependence of the true attenuation. Panel (e) shows severe bias in the fitted b because of the spurious rollover. The bias is so severe that it seems strange to even attempt fitting $\alpha = af^b$, yet this is retained as an illustration of the problem. These results are similar to the rollovers reported in (Li et al., 2017), though that study attributes the rollovers to wind input. Here, the noise bias causes a spurious rollover that shifts to lower frequencies at longer distances; that pattern is qualitatively consistent with rollover patterns reported in Li et al. (2017). In panel (d), the observed wave heights continue to agree well with the true wave heights because H_n is small.

We can repeat the approach of Meylan et al. (2014), who analyzed the actual field observations using a constant cutoff $E(f) > 10^{-2}$ m²/Hz that is well above the imposed $E_n(f)$ at any frequency. That applies a

constraint $\frac{E_n(f)}{E(f,x)} \ll \frac{1}{10}$ at all frequencies, as is shown by the faint horizontal line in panels (a) and (b)

of Figure 6. With this new constraint, the synthetic observations no longer have much rollover in observed attenuation rates (not shown). However, the cutoff creates severe limitations on the frequencies f that can be analyzed at any particular distance x . The higher frequencies ($f > 0.15$ Hz) have energies below the cutoff at all x , and thus no attenuation values are calculated for those frequencies.

3.5. STIMPI 2000

The Weddell Sea STIMPI 2000 case study results are shown in Figure 7. The specified noise energy clearly affects the observed spectra in panel (b), relative to the true spectra in panel (a). In panel (c), the noise bias causes spurious rollovers in the observed attenuation rates which are similar to the rollovers reported in the Li et al. (2017) analysis of the actual field data. The fitted exponent shown in panel (e) rapidly deviates

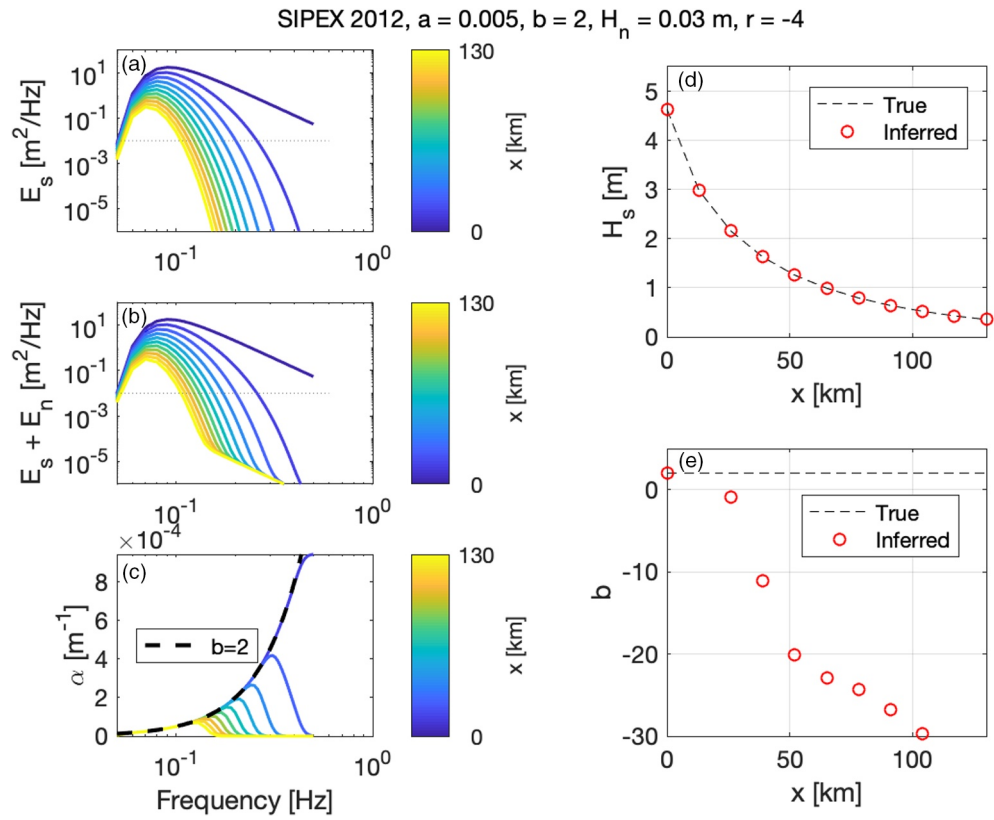


Figure 6. Synthetic results for the Antarctic SIPEX 2012 case study. Panels as in Figure 4. The gray dotted line in (a) and (b) shows the cutoff used in Meylan et al. (2014), which avoided spurious rollover in attenuation because it was well above the noise at all frequencies.

from the true b because the noise bias is sufficient to cause the apparent rollover. For both of these cases addressed in Li et al. (2017), it may be that noise bias and wind input contribute together in producing apparent rollovers in attenuation rates. Again, in panel (d), the observed wave heights agree well with the true wave heights.

3.6. Greenland Sea 1978

The Greenland Sea 1978 case study results are shown in Figures 8 and 9. Two figures are used for this case as a way to explore the effects of different noise shapes $r = 0$ and $r = -4$ because actual shape is not known. For either, the noise is sufficient to cause spurious rollovers in the inferred attenuation. The effect is worse for $r = 0$, though either result is qualitatively consistent with the rollovers in Figure 5a of Wadhams et al. (1988). Again, there is almost no bias in the wave heights inferred in this case study.

4. Discussion

Results suggest that negative bias in attenuation rates at high frequencies is a common issue for most field observations. Along with wind input and nonlinear mechanisms that may affect the high-frequency tail of ocean wave spectra, spurious energy from instrument noise is an explanation for all of the rollovers in attenuation that have been reported in the literature.

The following guidelines are recommended for future use of field observations in the estimation of spectral attenuation rates:

- Do not apply a constant cutoff in spectral wave energy, as this implies a flat noise spectrum ($r = 0$) that is unlikely for most observations

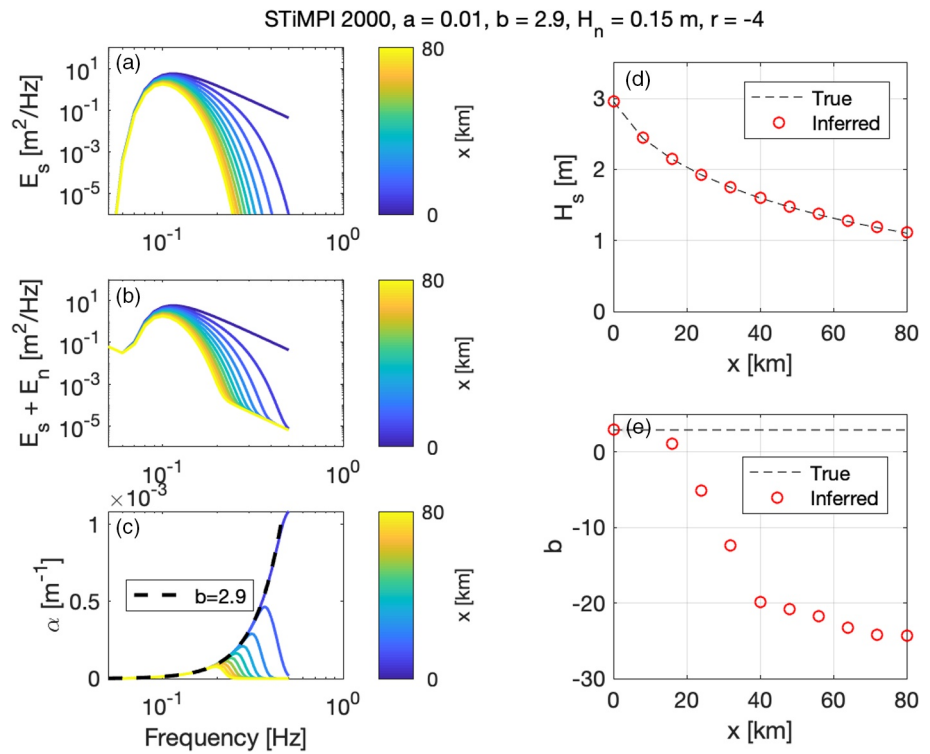


Figure 7. Synthetic results for the Weddell Sea STiMPI 2000 case study. Panels as in Figure 4.

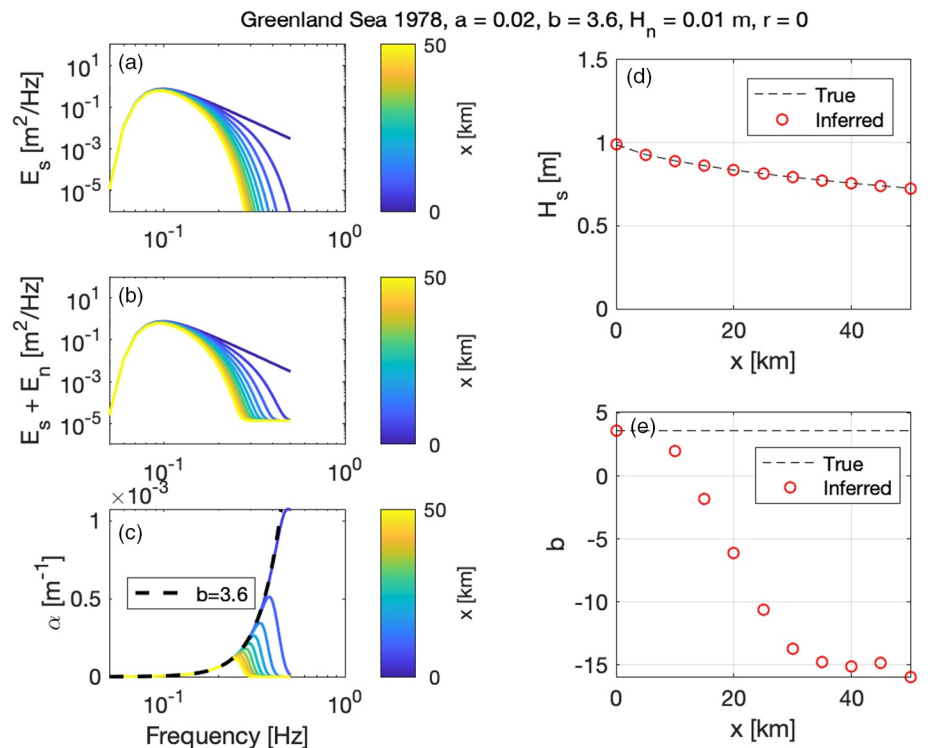


Figure 8. Synthetic results for the Greenland Sea 1978 case study, with spectral noise exponent $r = 0$. Panels as in Figure 4.

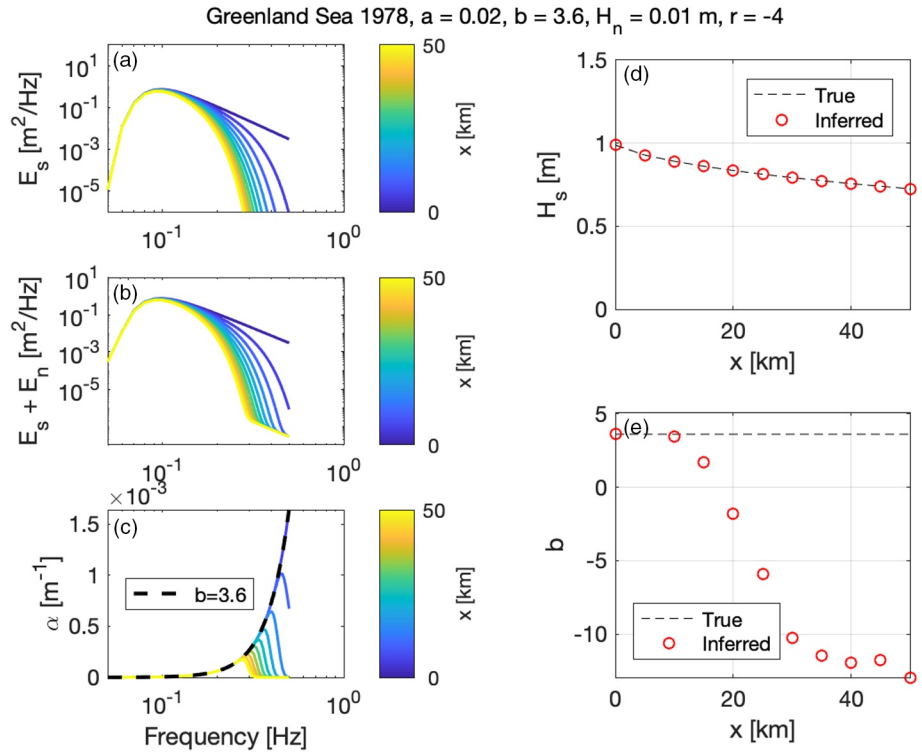


Figure 9. Synthetic results for the Greenland Sea 1978 case study, with spectral noise exponent $r = -4$. Panels as in Figure 4.

- Determine the spectral shape of the noise empirically, including any filters used in postprocessing and the deployment specifics
- Consider the ratio $E_n(f)/E_s(f, x)$ as a function of frequency and location, and avoid calculations of attenuation for *any* observation with appreciable $\frac{E_n(f)}{E(f, x)}$
- Check for convergence of attenuation results applying minimum $E(f)$ cutoffs as $\frac{E_n(f)}{E(f, x)} \rightarrow 0$

The deployment specifics in the second point are particularly important, given the common practice of placing wave measurement devices on ice floes. The hydrodynamic response of ice floes will depend on their dimensions and mass, such that they may have a damped response at high frequencies and the noise floor may be elevated relative to testing a device floating in open water. The frequencies affected can be estimated following the methods of Thomson et al. (2015), who report on the analogous condition of a wave buoy with a dramatic increase in size resulting from biofouling.

It is important to restate that the noise bias reported herein has a negligible effect on the total energy (and thus wave heights). Bulk attenuation rates can be determined robustly, even in the presence of noise. It is the spectral tail (high frequencies) in which much care is required.

4.1. Noise Effects at Low Frequencies

Although the focus herein is on high frequencies, energy from noise also can bias attenuation results at low frequencies. As shown in Figure 1, the f^{-4} shape may persist at low frequencies, though the actual level may vary depending on filters applied to reduce drift in the raw accelerometer data. We thus include a brief investigation of low-frequency noise bias by recalculating the attenuation coefficients from SIPEX 2012, as published in Meylan et al. (2014).

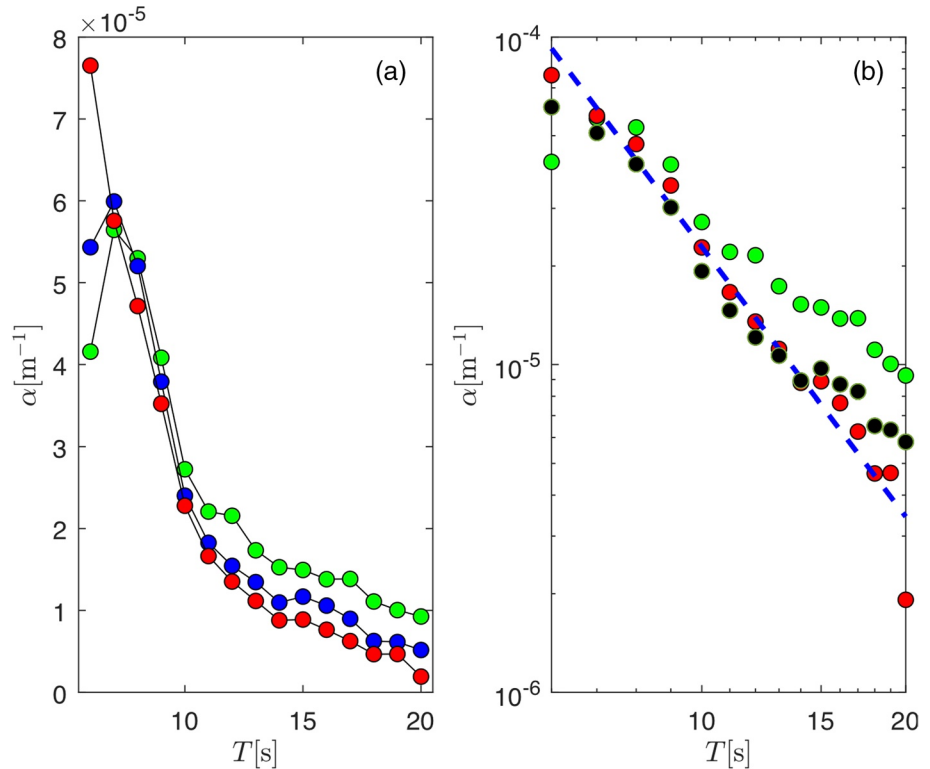


Figure 10. (a) Median low-frequency attenuation rates from SIPEX as a function of wave period applying noise cutoffs of $E(f)f^{-4} < 10^{-8}$ (green dots), $E(f)f^{-4} < 10^{-7}$ (blue dots), and $E(f)f^{-4} < 10^{-6}$ (red dots). (b) The median attenuation rates for $E(f)f^{-4} < 10^{-8}$ (green dots), the median attenuation rates for $E(f)f^{-4} < 10^{-6}$ (red dots) (which is the correct noise floor shown in Figure 1) and the results from the previous analysis in (Meylan et al., 2014) (black dots). The blue dotted line is the straight line fit to the red dots, $\alpha(f) \sim f^b$.

We note that the original data analysis in Meylan et al. (2014) was based on a frequency independent noise cut off ($r = 0$). In that analysis, the noise floor was set sufficiently high to avoid the roll over; indeed, no analysis was completed for any periods $T < 6$ s (or $f > 0.15$ Hz). Although sufficiently conservative to avoid spurious calculations in the high-frequency tail, this cutoff had a secondary effect of removing measurements at low frequencies (long periods). An empirical determination of the noise energy at these frequencies is elusive and beyond the scope of this manuscript. Rather, we simply explore the implications of different choices applying a noise cutoff at low frequencies. Figure 10 shows the sensitivity to the noise cutoff by comparing the median attenuation with a fixed noise floor cutoff ($r = 0$, as used in Meylan et al., 2014) and using three different levels of noise floor cutoffs that are empirical power laws in frequency ($r = -4$).

The left panel of Figure 10 show attenuation results with three different levels of f^{-4} cutoff applied. The right panels show the median attenuation as a function of period for the two of the three levels. The black curves are from the original analysis of Meylan et al. (2014), for comparison. The constant noise floor applied in original analysis lowered the attenuation at short periods and raised it at long periods. The correct analysis is the lower right panel, and the blue line is the fit to the power law. This analysis suggests a power law with $b = 3$ for the true attenuation, which is within the range of expected exponents (Meylan et al., 2018).

Just as the negative bias in attenuation rate at high frequencies results from exponents $r - q > 0$, the positive bias in attenuation rate at low frequencies is the consequence of $r - q < 0$. At these low frequencies, the noise energy $E_n(f)$ is more steep than the signal energy $E_s(f)$ because the signal is outside of the equilibrium wind wave range. The general result is the same: the frequency dependence of the attenuation rates will be sensitive to the noise cutoff, even when the absolute error in the attenuation rates is small.

5. Conclusions

Instrument noise in wave measurements causes a bias in attenuation rates that manifests in spurious relations between frequency and attenuation rates. This is sufficient to explain the rollover in attenuation rates observed for several studies from a variety of different wave-ice buoys. A general form of the noise bias (Equation 8) can be applied to avoid this issue in future analysis.

Data Availability Statement

The CODA project is detailed at <http://www.apl.uw.edu/coda>, and the CODA 2019 data are available at <http://hdl.handle.net/1773/46587>. The Arctic Sea State project is detailed at <http://www.apl.uw.edu/arctic-seastate>, and the 2015 data are available at <http://hdl.handle.net/1773/41864>. SIPEX data are available at <https://doi.org/10.4225/15/53266BEC9607F>. STIMPI were provided by Martin Doble (Polar Scientific, Ltd.).

Acknowledgments

Funded by the National Science Foundation (OPP-1818485) as part of the Coastal Ocean Dynamics in the Arctic project. Erick Rogers provided valuable feedback and discussions during the preparation of the manuscript. Two anonymous reviewers helped improve the manuscript and motivated the inclusion of the Greenland Sea 1978 case study.

References

- Alves, J. H. G. M., Banner, M. L., & Young, I. R. (2003). Revisiting the Pierson–Moskowitz asymptotic limits for fully developed wind waves. *Journal of Physical Oceanography*, 33(7), 1301–1323. [https://doi.org/10.1175/1520-0485\(2003\)0331301:RTPALF2.0.CO;2](https://doi.org/10.1175/1520-0485(2003)0331301:RTPALF2.0.CO;2)
- Ardhuin, F., Otero, M., Merrifield, S., Grouazel, A., & Terrill, E. (2020). Ice break-up controls dissipation of wind-waves across southern ocean sea ice. *Geophysical Research Letters*, 47, e2020GL087699. <https://doi.org/10.1029/2020GL087699>
- Banner, M. L. (1990). Equilibrium spectra of wind waves. *Journal of Physical Oceanography*, 20, 966–984.
- Cheng, S., Rogers, W. E., Thomson, J., Smith, M., Doble, M. J., Wadhams, P., et al. (2017). Calibrating a viscoelastic sea ice model for wave propagation in the arctic fall marginal ice zone. *Journal of Geophysical Research: Oceans*, 122. <https://doi.org/10.1002/2017JC013275>
- Doble, M. J., De Carolis, G., Meylan, M. H., Bidlot, J.-R., & Wadhams, P. (2015). Relating wave attenuation to pancake ice thickness, using field measurements and model results. *Geophysical Research Letters*, 42(11), 4473–4481. <https://doi.org/10.1002/2015GL063628>
- Herbers, T. H. C., Jessen, P. F., Janssen, T. T., Colbert, D. B., & MacMahan, J. H. (2012). Observing ocean surface waves with GPS tracked buoys. *Journal of Atmospheric and Oceanic Technology*, 29. <https://doi.org/10.1175/JTECH-D-11-00128.1>
- Hosekova, L., Malila, M. P., Rogers, W. E., Roach, L. A., Eidam, E., Rainville, L., et al. (2020). Attenuation of ocean surface waves in pancake and frazil sea ice along the coast of the chukchi sea. *Journal of Geophysical Research: Oceans*, 125(12), e2020JC016746. <https://doi.org/10.1029/2020JC016746>
- Kohout, A. L., Penrose, B., Penrose, S., & Williams, M. J. (2015). A device for measuring wave-induced motion of ice floes in the antarctic marginal ice zone. *Annals of Glaciology*, 56(69), 415–424. <https://doi.org/10.3189/2015AoG69A600>
- Kohout, A. L., Williams, M. J. M., Dean, S. M., & Meylan, M. H. (2014). Storm-induced sea-ice breakup and the implications for ice extent. *Nature*, 509, 604. <https://doi.org/10.1038/nature13262>
- Lenain, L., & Melville, W. K. (2017). Measurements of the directional spectrum across the equilibrium saturation ranges of wind-generated surface waves. *Journal of Physical Oceanography*, 47(8), 2123–2138. <https://doi.org/10.1175/JPO-D-17-0017.1>
- Li, J., Kohout, A. L., Doble, M. J., Wadhams, P., Guan, C., & Shen, H. H. (2017). Rollover of apparent wave attenuation in ice covered seas. *Journal of Geophysical Research: Oceans*, 122, 8557–8566. <https://doi.org/10.1002/2017JC012978>
- Masson, D., & LeBlond, P. (1989). Spectral evolution of wind-generated surface gravity waves in a dispersed ice field. *Journal of Fluid Mechanics*, 202(111), 43–81.
- Meylan, M. H., Bennetts, L. G., & Kohout, A. L. (2014). In situ measurements and analysis of ocean waves in the Antarctic marginal ice zone. *Geophysical Research Letters*, 41(14), 5046–5051. <https://doi.org/10.1002/2014GL060809>
- Meylan, M. H., Bennetts, L. G., Mosig, J. E. M., Rogers, W. E., Doble, M. J., & Peter, M. A. (2018). Dispersion relations, power laws, and energy loss for waves in the marginal ice zone. *Journal of Geophysical Research: Oceans*, 123(5), 3322–3335. Retrieved from <https://agupubs.onlinelibrary.wiley.com/doi/abs/10.1002/2018JC013776>
- Phillips, O. M. (1985). Spectral and statistical properties of the equilibrium range in wind-generated gravity waves. *Journal of Fluid Mechanics*, 156, 495–531.
- Polnikov, V. G., & Lavrenov, I. V. (2007). Calculation of the nonlinear energy transfer through the wave spectrum at the sea surface covered with broken ice. *Oceanology*, 47(3), 334–343. <https://doi.org/10.1134/S0001437007030058>
- Rogers, W. E., Thomson, J., Shen, H. H., Doble, M. J., Wadhams, P., & Cheng, S. (2016). Dissipation of wind waves by pancake and frazil ice in the autumn beaufort sea. *Journal of Geophysical Research: Oceans*, 121(11), 7991–8007. <https://doi.org/10.1002/2016JC012251>
- Squire, V. A. (2007). Of ocean waves and sea ice revisited. *Cold Regions Science and Technology*, 49, 110–133.
- Squire, V. A. (2020). Ocean wave interactions with sea ice: A reappraisal. *Annual Review of Fluid Mechanics*, 52(1), 37–60. <https://doi.org/10.1146/annurev-fluid-010719-060301>
- Sutherland, P., Brozena, J., Rogers, W. E., Doble, M., & Wadhams, P. (2018). Airborne remote sensing of wave propagation in the marginal ice zone. *Journal of Geophysical Research: Oceans*, 123(6), 4132–4152. Retrieved from <https://agupubs.onlinelibrary.wiley.com/doi/abs/10.1029/2018JC013785>
- Thomson, J. (2012). Wave breaking dissipation observed with SWIFT drifters. *Journal of Atmospheric and Oceanic Technology*, 29(12), 1866–1882. <https://doi.org/10.1175/JTECH-D-12-00018.1>
- Thomson, J., Ackley, S., Girard-Ardhuin, F., Ardhuin, F., Babanin, A., Boutin, G., et al. (2018). Overview of the arctic sea state and boundary layer physics program. *Journal of Geophysical Research: Oceans*, 123(12), 8674–8687. <https://agupubs.onlinelibrary.wiley.com/doi/abs/10.1002/2018JC013766>
- Thomson, J., D'Asaro, E. A., Cronin, M., Rogers, E., Harcourt, R., & Scherbinska, A. (2013). Waves and the equilibrium range at Ocean Weather Station P. *Journal of Geophysical Research*, 118, 1–12. <https://agupubs.onlinelibrary.wiley.com/doi/full/10.1002/2013JC008837>
- Thomson, J., Giron, J. B., Jha, R., & Trapani, A. (2018). Measurements of directional wave spectra and wind stress from a wave glider autonomous surface vehicle. *Journal of Atmospheric and Oceanic Technology*, 35(2), 347–363. <https://doi.org/10.1175/JTECH-D-17-0091.1>

- Thomson, J., Talbert, J., de Klerk, A., Brown, A., Schwendeman, M., Goldsmith, J., et al. (2015). Biofouling effects on the response of a wave measurement buoy in deep water. *Journal of Atmospheric and Oceanic Technology*, *32*(6), 1281–1286. <https://doi.org/10.1175/JTECH-D-15-0029.1>
- Vincent, C. L., Thomson, J., Graber, H. C., & Collins, C. O. (2019). Impact of swell on the wind-sea and resulting modulation of stress. *Progress in Oceanography*, *178*, 102164. <https://doi.org/10.1016/j.pocan.2019.102164>
- Wadhams, P. (1975). Airborne laser profiling of swell in an open ice field. *Journal of Geophysical Research*, *80*(33), 4520–4528. Retrieved from <https://agupubs.onlinelibrary.wiley.com/doi/abs/10.1029/JC080i033p04520>
- Wadhams, P., Squire, V. A., Goodman, D. J., Cowan, A. M., & Moore, S. C. (1988). The attenuation rates of ocean waves in the marginal ice zone. *Journal of Geophysical Research*, *93*(C6), 6799–6818.